Heliyon 9 (2023) e20264

Contents lists available at ScienceDirect

Heliyon

journal homepage: www.cell.com/heliyon

Anti-reflection effect of high refractive index polyurethane with different light trapping structures on solar cells

Shengxuan Wang [a], Hao Cui [a], Sijia Jin [a], Xiaodong Pi [a,c], Haiyan He [b], Chunhui Shou [b,**], Deren Yang [a], Lei Wang [a,*]

[a] State Key Laboratory of Silicon and Advanced Semiconductor Materials, School of Materials Science and Engineering, Zhejiang University, Hangzhou 310027, China
[b] Zhejiang Baima Lake Laboratory Co., Ltd., Hangzhou Zhejiang 310000, China
[c] Institute of Advanced Semiconductors and Zhejiang Provincial Key Laboratory of Power Semiconductor Materials and Devices, Hangzhou Innovation Center, Zhejiang University, Hangzhou 311200, China

ARTICLE INFO

Keywords:
Anti-reflection
Soft nanoimprint lithography
High refractive index polyurethane
Light trapping structure
Theoretical simulation

ABSTRACT

The textured surfaces to reduce light reflectivity by using acid-alkali chemical etching and SiN_x films are generally necessary for commercial crystalline silicon solar cells. However, this etching process requires a large amount of environmentally harmful acid-alkali solution and has limited options for texture and size. To overcome these disadvantages, a new anti-reflection strategy is proposed in this study, which is using soft nanoimprint lithography to prepare the textured structures on the outside of the SiN_x films. The polyurethane with a high refractive index of 1.64 is selected as the texture material, and different templates are selected to prepare it into different light trapping structures, including positive-inverted pyramids, inverted lace cones, and positive-inverted moth-eye nanostructures allowing for easy customization of the textured structures. The finite element simulation and experiments demonstrate that these light trapping structures have a wide spectrum anti-reflection performance in visible and near-infrared bands. With the back surface of the commercial passivated emitter rear contact (PERC) bi-facial solar cells as the imprint substrates, some light trapping structures can reduce the surface weighted average light reflectivity (R_w) at the band of 300–1200 nm from 18.31% to less than 10% and the optimal structures can reduce R_w to 8.71%. This anti-reflection strategy can also be applied to thin-film solar cells and crystalline silicon solar cells of other structures, such as HIT, Topcon, Perovskite/c-Si tandem, and so forth, which shows great development potential.

1. Introduction

In the context of the global energy crisis, the development of green renewable energy is crucial. Solar energy, as a clean and inexhaustible energy source, is increasingly popular due to its ability to convert light into electricity directly through the photovoltaic effect. The photovoltaic industry has grown significantly in recent years as technology has improved and the levelized cost of electricity(LCOE) has decreased [1]. At present, crystalline silicon solar cells still account for more than 90% of the market share in the

* Corresponding author.
** Corresponding author.
E-mail addresses: shouchunhui@zjenergy.com.cn (C. Shou), phy_wangl@zju.edu.cn (L. Wang).

https://doi.org/10.1016/j.heliyon.2023.e20264
Received 31 August 2023; Received in revised form 12 September 2023; Accepted 17 September 2023
Available online 19 September 2023

photovoltaic industry because of their higher conversion efficiency and longer service life. Meanwhile, thin film solar cells such as amorphous silicon solar cells, perovskite solar cells, CIGS solar cells, CdTe solar cells, and others, which have broad application prospects in flexible photovoltaic devices and photovoltaic building integration, are also developing rapidly [2].

To improve the absorption rate of sunlight, it is necessary to prepare an anti-reflection structure on both crystalline silicon and thin film solar cells [3]. Currently, the most common method for preparing an anti-reflection structure on crystalline silicon solar cells is to use a light trapping texture combined with a SiN_x anti-reflection film. This process involves using acid or alkali to etch the silicon and make a light trapping structure that reduces the reflection loss of incident sunlight, thereby increasing the short-circuit current. Alkali etching can be used to prepare positive or inverted pyramid structures for mono-crystalline silicon, which are composed of the {111} crystal plane group and have a good light trapping effect [4]. However, due to the saw-marks on the surface and the irregularity of the crystal phase, uniform anti-reflection structures cannot be prepared using alkali etching for the multi-crystalline silicon. So acid etching is often used to enhance the light trapping effect [5]. The etching process has two major disadvantages: (1) the use of large amounts of corrosive alkali or acid results in waste and increment of production costs, and (2) the etching process increases the specific surface area of the silicon wafers, leading to increased surface recombination and, consequently, a decrease in both short circuit current and open circuit voltage [6].

To address the above issues, our approach is to use soft nanoimprint lithography instead of acid-alkali etching to prepare various textured structures after coating the flat silicon wafers with a SiN_x anti-reflection film. Soft nanoimprint lithography is a convenient and inexpensive lithographic pattern transfer technology that is currently a hot topic in research [7]. It can be used to texture surfaces with various morphologies to reduce light reflectivity, such as positive-inverted nanocones [8–10], nanopillars [11], positive-inverted pyramids [12–14], positive-inverted moth-eye nanostructures [15–17], nanothorns [18], and so forth. The anti-reflection structures, built on the SiN_x film, can be more complex and efficient than traditional pyramid structures because they are not limited by chemical etching.

The SiN_x anti-reflection film is essential because it not only reduces light reflectivity but also passivates the surface of silicon wafers [19]. The refractive index of a SiN_x anti-reflection film generally exhibits a gradient, decreasing from the surface of silicon wafers outward, and the refractive index of its outermost layer is generally about 1.9. According to the Fresnel reflection law, to minimize light reflectivity for the entire solar cells, the value of the refractive index for the texturing material should be between that of the outermost layer of the SiN_x (refractive index of 1.9) and that of the packaging materials(approximate refractive index of 1.5 for the Ethylene Vinyl Acetate (EVA)). In addition to matching the refractive index, the material should have a low absorption coefficient and high transmittance. Materials can be considered from two perspectives: inorganic and organic. Inorganic materials that meet these requirements include Al_2O_3 [20], ZnO, and the like. In our previous work, we had constructed a ZnO nano-needle array on the surface of the multi-crystalline silicon surface to achieve good light trapping effect [21]. However, the preparation of such inorganic oxide nanostructures is a complex and costly method, and it is impossible to form customized structures by self-assembly method. Therefore, it may be a better choice to use organic materials to construct light trapping structures. Organic materials include some high refractive index, high transmittance modified polyesters, polyenes, and so on. Commonly used methods of modification include nanoparticle modification [22,23] and molecular modification [24,25], etc.

Based on these criteria, the high refractive index polyurethane(PU) suitable for soft nanoimprint lithography is selected. As a potential material for new lenses, it has a high refractive index, low absorption coefficient, high transmittance, and low cost of mass production [26]. In this article, it is imprinted as positive-inverted pyramid structures, inverted lace cone structures, and positive-inverted moth-eye nanostructures on the surface of non-textured mono-crystalline silicon solar cells, which are expected to further reduce the light reflectivity due to their appropriate refractive index and specialized light trapping structures.

COMSOL multiphysics field simulation can assist various theoretical and practical studies of solar cells, helping to analyze mechanisms and save experimental costs. For the light management of solar cells, the light trapping effects of different textured surfaces including nanocones [27], nanowires [28], and other structures, the plasmonic excitation effect of metal nanoparticles [29], and the light conversion properties of upconversion materials [30] can be simulated. Additionally, some other novel light trapping materials and theories are also expected to be applied to solar cells, such as graphene-embedded photonic crystals to realize ultra-broadband absorption [31], the use of gravitational field modulation to realize metamaterial absorbers [32] and the use of surface plasmon polariton to form novel waveguide structures [33].

In this article, we chose the backside of the commercial PERC bi-facial solar cells as the substrates because they have been polished and coated by SiN_x anti-reflection films [34], which can be used to verify the effect of the anti-reflection strategy we designed. COMSOL multiphysics field optical simulations are utilized to further investigate the anti-reflection mechanisms of the structures [35].

2. Material and methods

The following materials were used in the study: ethanol(Aladdin), hydrochloric acid(SCR), triethoxy-1H,1H,2H,2H-tridecafluoro-*n*-octylsilane(Aladdin), *m*-Xylylene Diisocyanate(XDI, Aladdin), dibutyltin dichloride(Aladdin), 4-Mercaptomethyl-3,6-dithia-1,8-octanedithiol (GST, Wengjiang reagent), epoxy resin glue (ER) and polydimethylsiloxane (PDMS, DC 184 DOW SIL). The original hard templates included anodized aluminum oxide (AAO) templates with conical holes of different sizes: diameter-height of 450–1500 nm (A1500), diameter-height of 450–900 nm (A900), and diameter-height of 450-400 nm (A400). Meanwhile, the commercial pyramid-textured solar cells were also original hard templates. Soft templates were prepared using PDMS, while synthetic ER templates could be used as hard templates. The commercial PERC bi-facial mono-crystalline silicon solar cells from *CHINT SOLAR* were used and cut into pieces (3 cm × 3 cm), with the rear as the substrate for soft nanoimprint lithography.

2.1. Anti-adhesive treatment for templates

For uniform anti-adhesive treatment of different soft and hard templates before imprinting, the following method was used: dilute triethoxy-1H,1H,2H,2H-tridecafluoro-*n*-octylsilane fluoride to 0.5 wt% in ethanol, add dilute hydrochloric acid (HCl) to adjust the pH of the solution to 4–5. Stir the solution for 10 min, then immerse the different soft and hard templates into the solution for 10 min. Remove residual solvent by deionized water and ultrasonic cleaning, then place the templates in an oven to dry. The operation flow is shown as Process 1 in Fig. 1.

2.2. Preparation of ER hard templates with different morphologies

To prepare the ER hard templates with different morphologies, the following method was used: mix the ER glue(main agent: curing agent = 3:1, mass ratio) and thoroughly stir. Transfer the mixture to a vacuum furnace and degas for 10 min. Pour the ER solution onto the anti-adhesion treated AAO templates or commercial pyramid-textured solar cell templates and cure at 60 °C for 3 h. After de-molding, the ER hard templates with positive conical structures or inverted pyramid structures can be obtained. The preparation process for the ER-positive cone hard templates is shown in Fig. 1(a)–(c) of process 2.

2.3. Preparation of PDMS soft templates

To prepare PDMS soft templates with different morphologies, DC184 was mixed (main agent: curing agent = 10:1, mass ratio) and thoroughly stirred. The mixture was then degassed in a vacuum oven at room temperature for 30 min. The mixed solution was then dripped onto the surface of hard templates with different morphologies that had undergone anti-adhesive treatment and cured at 60 °C for 6 h in a vacuum oven. PDMS was then lifted off to obtain the soft templates. The preparation process is shown in Fig. 1(c)–(e) of process 2.

2.4. Preparation of PU anti-reflection structures

To prepare an uncured PU solution, we follow the method described by Zhang Guiming [36]: add 2 mg of dibutyltin dichloride to 1 g of XDI, and stir at room temperature for 10 min. Then, add 0.2 g of the resulting mixture to 1.19 g of XDI and stir in an ice bath for 10 min. Keep the mixture in the ice bath and add 1.28 g of GST, stirring for an additional 5 min. Transfer the mixture to a vacuum furnace

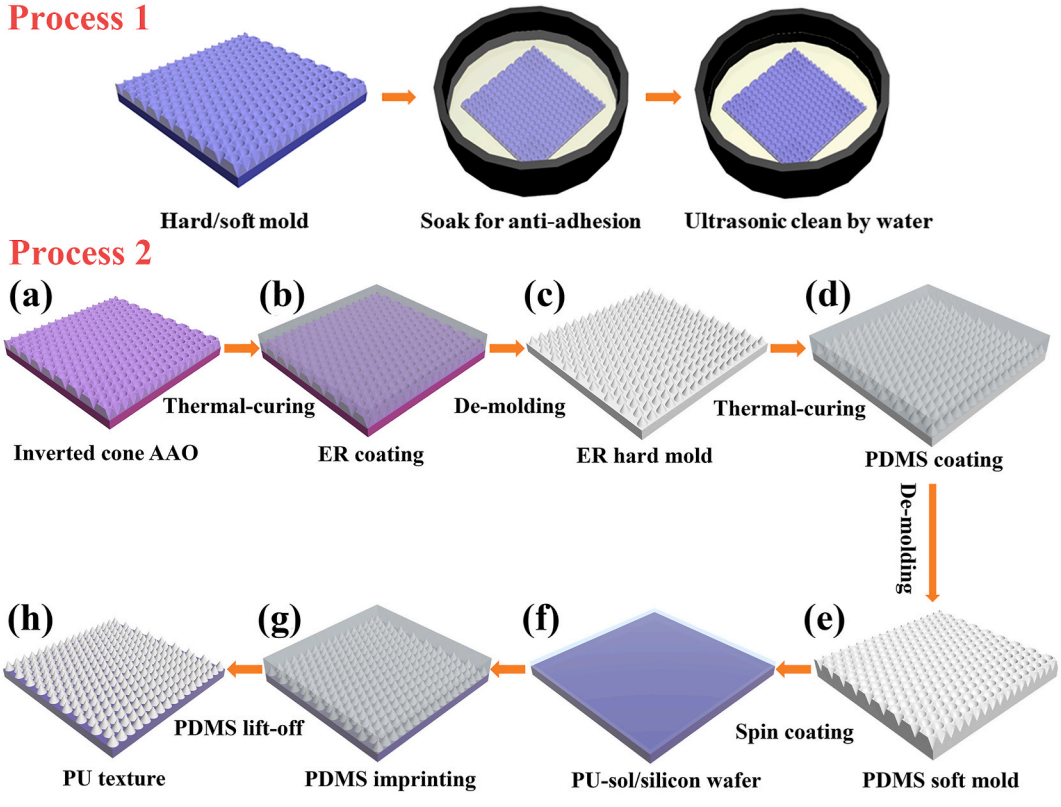

Fig. 1. Schematic diagram of the soft nanoimprint lithography process.

and degas for 30 min to obtain an uncured PU solution with a molar ratio GST: XDI = 2:3.

The backside of the commercial PERC bi-facial solar cells was used as the substrates for soft nanoimprint lithography. The solar cells were cleaned by ultrasonic in a mixed solution with a volume ratio of acetone: ethanol: H_2O = 1: 1: 1 and DI water for 15 min respectively. After drying, the PU solution was spin-coated onto the surface of the solar cells at a rotational speed of 1000 RPM. After 10 s, the anti-adhesive PDMS soft templates were imprinted onto the surface of the PU solution, applying a pressure of 10 N to allow sufficient infiltration. The coated solar cells were then placed in a vacuum drying oven and cured for 2 h at a temperature of 120 °C. The textured PU surface was obtained after removing the PDMS. The preparation diagram for the PU-positive conical morphology is shown in Fig. 1(e)–(h) of process 2.

2.5. Test methods

A scanning electron microscope (GeminiSEM 300, Zeiss) was used to observe the surface morphology of the sample. A UV–Vis–NIR spectrophotometer (HITACHI U-4100) was used to measure the light reflectivity of the sample at the band of 300–1200 nm. The light reflectivity was weighted with the number of photons in the AM1.5G spectrum [37] to calculate the weighted average light reflectivity (R_w). The refractive index of PU was measured by an elliptic polarization spectrometer (M − 2000, J.A. Woollam). In addition, a quantum efficiency measurement instrument (QEX10) was used to measure the external quantum efficiency(EQE) of the sample at the band of 300–1200 nm to characterize the effect of anti-reflection on the electrical performance of solar cells.

2.6. COMSOL multiphysics simulation

According to the texture morphologies observed by SEM, COMSOL Multiphysics field simulation was used for modeling, the optical module wavelength domain module was used for optical simulation, and its electrical modulus and global reflectivity were calculated.

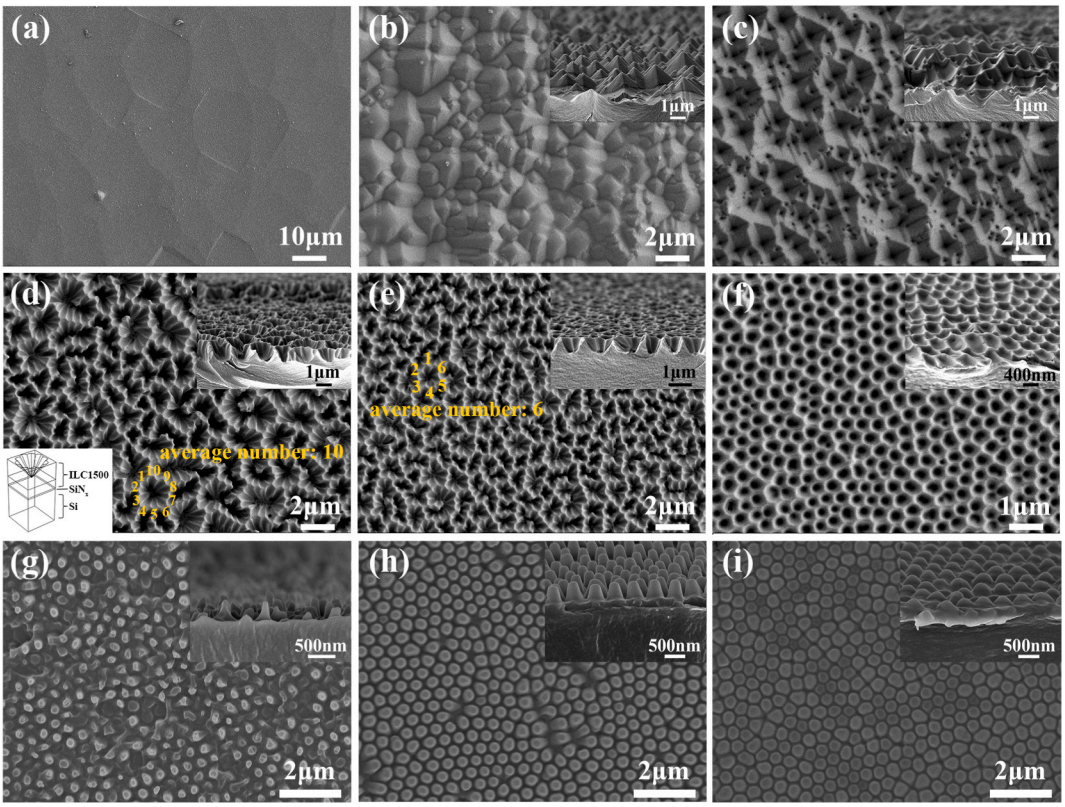

Fig. 2. SEM images of different morphologies of solar cells' surface and cross-sectional(inset images). (a) shows the surface of the backside of PERC bi-facial solar cells, (b) and (c) show the morphologies of PUs with positive and inverted pyramids, respectively, (d) and (e) respectively show the SEM images of PUs with inverted lace conical morphologies transferred from A1500 and A900, (g) and (h) respectively show the SEM images of PUs with positive moth-eye nanostructures transferred from A1500 and A900, (f) and (i) show the morphologies of PUs with inverted and positive moth-eye nanostructures transferred from A400, respectively.

3. Results and discussion

Texturing the surface of silicon wafers is a crucial process to improve their anti-reflection properties. As seen in Fig. 2(a), the silicon wafers after alkaline polishing present small protrusions and depressions that do not impact the effect of soft nanoimprint lithography. As illustrated in Fig. 2(b) and (c), the PUs with micrometer-level positive or inverted pyramids (PPY and IPY) transferred from the commercial pyramid-textured solar cell templates present sharp edges and angles, achieving a better pattern transfer. When light is incident on the convex or concave pyramid structure, multiple reflections and refractions are produced, increasing the proportion of light that enters the silicon substrates, which in turn improves photocurrent gains. Fig. 2(d) and (e) show the inverted lace cones 1500 nm and 900 nm (ILC1500 and ILC900) imprinted by A1500 and A900 transfer. The formation of lace is a result of small-scale agglomeration that occurs after de-molding the PDMS soft templates from the hard templates. An increase in the aspect ratio of the cone structures leads to a higher number of agglomeration events. The average number of reunions for ILC1500 is about 10 and for ILC900 is about 6. The average opening diameter of ILC1500 is 1.8 μm and the average depth is 1 μm, meanwhile, the average opening diameter of ILC900 is 1.3 μm and the average depth is 650 nm. Furthermore, the structure transferred from A400 does not agglomerate, instead, it forms an inverted moth-eye nanostructure(IME400), as shown in Fig. 2(f). This is due to the small length-to-diameter ratio of the cone structures and the increased distance between cones, which make it difficult for them to adsorb together. The average opening diameter is 450 nm and the average depth is 200 nm. As shown in Fig. 2(g), (h), and (i), the structures produced by the inverted cone of A1500, A900, and A400 are transferred twice. Instead of being aggregated into the lace cones, they are transferred into the positive moth-eye nanostructures of different sizes, named PME1500, PME900, and PME400, respectively. The reason for this is that the inverted cone structures of PDMS soft templates do not aggregate. The dimensions of PME1500, PME900, and PME400 are measured with bottom diameters of about 450 nm, and heights of approximate 500 nm, 450 nm, and 200 nm, respectively.

The results of the soft nanoimprint lithography process demonstrate that micron-scale structures are successfully transferred with high accuracy, whereas, nano-scale structures experienced different degrees of collapse. With the height collapse rate as the evaluation index, the collapse rates are calculated for different nano-scale structures(Table 1). The collapse rates for nanostructures with high heights increase after a double transfer, but the collapse rates for nanostructures with lower heights are not affected. This can be attributed to the large contact angle between the transfer glue and the hydrophobically treated template, resulting in incomplete infiltration of the transfer glue into deep nanostructures. But if there is no anti-adhesive treatment, the templates can not be de-molded. To improve the transfer accuracy, the vacuum level should be increased in the embossing chamber to remove any residual bubbles in the templates.

At the same time, the refractive index of the selected material needs to match the upper and lower interfaces. In this article, a high refractive index PU containing benzene ring and -S- is prepared. The refractive index of the PU at a wavelength of 500 nm is determined to be 1.64 using ellipsometric spectroscopy (Fig. 3(a)). This value falls between that of SiN_x (1.9) and EVA (1.5). According to the Huygens-Fresnel principle, when the refractive index difference between the two interfaces decreases, the total reflectance will correspondingly decrease. The intermediate layer of PU divides the large refractive index difference between the SiN_x and EVA interfaces into two smaller refractive index differences, which contributes to a reduction in overall reflectivity. The polymerization reaction equation of the monomers XDI and GST is as shown in Fig. 3(b). The polymerized PU contained a large number of benzene rings, sulfide bonds, and –CO–NH- bonds, which contribute to its high refractive index. The molar refractive index of the benzene ring, the sulfide bond, and the –CO–NH- bond are 25.46, 7.92, and 7.23, respectively [38].

The backside of PERC bi-facial solar cells (blank group) are used as examples to reflect the effect of the anti-reflection structures in this article. They have flat SiN_x anti-reflection films with the refractive index of 1.9 (500 nm) and the thickness of about 120 nm. The reflectance spectrum of various structures is measured using a UV–Vis–NIR spectrophotometer and the R_w is calculated. The results are shown in Table 2. The reflectance spectrum of the various light trapping structures on the rear is shown in Fig. 4(a)-(d). It can be seen that all structures have certain anti-reflection effects across the wide spectrum. The micron-scale positive-inverted pyramid, ILC1500, and ILC900 structures due to their micron-scale sizes, mainly achieved the light trapping effect through multiple reflections and refractions of incident light. The sizes of the PME1500, PME900, and P-IME400 are in the nano wavelength range, and according to the effective medium theory [39], they can function as multilayer anti-reflection films with a gradual refractive index, which has a broad spectrum anti-reflection effect. Some light trapping structures can reduce the R_w from 18.31% to less than 10% and the optimal ILC1500 structure can be reduced to as low as 8.71%, a 52.43% decrease. Of course, these structures can also be applied to the front side of non-textured crystalline silicon and thin film solar cells to produce an excellent anti-reflection effect.

It can be seen that the anti-reflection effect of the PPY structures is superior to that of the IPY structures. This is because the IPY structures have undergone twice transfer processes, leading to an increase in the collapse rate and a decrease in structural integrity.

Table 1
Sizes and height collapse rates of morphologies after transfer of different nanostructures.

Name	ILC1500	ILC900	IME400	PME1500	PME900	PME400
Average diameter of opening/base (nm)	1800	1300	450	450	450	450
Average depth/height (nm)	1000	650	200	500	450	200
Height collapse rate (%)	33.3	27.8	50	66.67	50	50

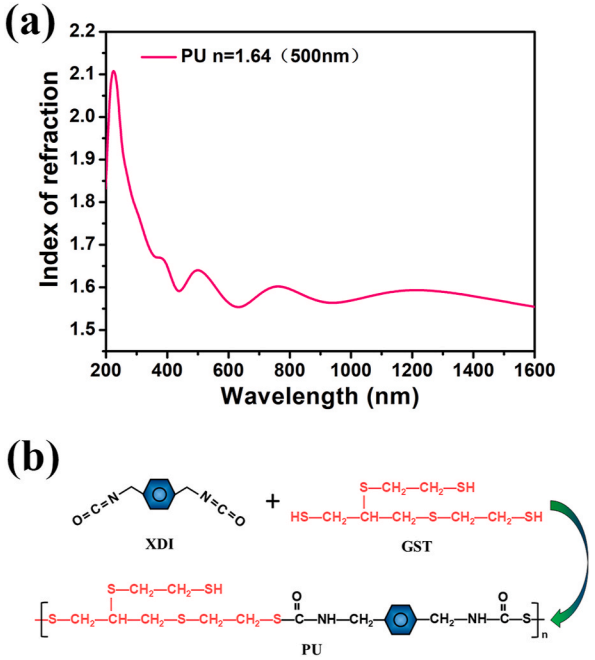

Fig. 3. (a) shows the refractive index of PU, (b) shows the equation of polymerization reaction of monomer XDI and GST.

Table 2
The weighted average light reflectivities of the surfaces of PU with different morphologies, the commercial soalr cells and the backside of PERC bi-facial solar cells (%).

Name	Blank group	Commercial	PPY	IPY	ILC 1500	ILC 900	IME 400	PME1500	PME 900	PME 400
Rear R_w	18.31	7.51	9.80	10.34	8.71	9.76	10.54	13.22	11.10	10.92
Rear R_w reduction rate	/	/	46.48	43.53	52.43	46.70	42.44	27.80	39.38	40.36

The anti-reflection effects of ILC1500 and ILC900 are better than that of PME1500 and PME900, respectively, for the same reason. The anti-reflection effects of PME400 and IME400 are similar, as the collapse rates of both are similar. All anti-reflection structures have a better anti-reflection effect in the 300–1000 nm band and a weaker effect in the 1000–1200 nm band. This is because the size of the prepared textured structures is equivalent to, or even smaller than, the long wavelength, and thus the effect of multiple reflection trapping cannot be achieved. Simultaneously, the refractive index of the anti-reflection structure also strongly influences the anti-reflection effect [40]. In future work, we intend to explore the use of materials with a higher refractive index to create textured structures, with the aim of achieving a better anti-reflection effect. For the optimal anti-reflection window in the 500–1000 nm band, it is mainly influenced by the refractive index and thickness of SiN_x, as well as the size and refractive index of the light trapping texture. This window can be adjusted by modifying the aforementioned parameters.

When comparing the surface reflection spectra of ILC1500 with those of commercial solar cells (front-side of the PERC bi-facial solar cell), it is evident that the light reflectivity of ILC1500 in the range of 300–1200 nm, is close to that of commercial soalr cells (Fig. 4(e)). Furthermore, the anti-reflection effect of ILC1500 in the short wavelength range of 300–450 nm outperforms that of commercial solar cells. Future enhancements in the morphology of the new anti-reflection structure are anticipated to achieve or even surpass the anti-reflection effect of commercial solar cells. Simultaneously, ILC1500 and blank group are packed with the glass coated with an anti-reflection film(AR-glass) and EVA, and the reflection spectrum is tested (Fig. 4(f)). The weighted average reflectance of packed ILC1500 is calculated to be 9.37%, which still has a better anti-reflection effect than the packed blank group($R_w = 10.30\%$). Compared with solar cells without packing, the reflectivity is increased because the reflection effect of the encapsulated glass and EVA interface is stronger than the composite anti-reflection effect. Comparing the different anti-reflection structures(Table 3), in the wide wavelength of 300–1200 nm, the present work ILC1500 has a good effect.

COMSOL multiphysics field simulation software is used to optically simulate the anti-reflection effect of ILC1500 and ILC900 structures, which are found to have better anti-reflection properties. The simulation model is shown in Fig. 5(a). From top to bottom, the model consists of a perfect matching layer (PML, height of 500 nm), air(height of 1000 nm), an inverted lace cone with a refractive index of 1.64, SiN_x film($n = 1.9$), Si substrate(height of 4000 nm), and PML(height of 500 nm). The electromagnetic waves from the upper interface of the air layer are vertically incident, and the upper and lower layers of PML are used to absorb the reflected or transmitted electromagnetic waves. The surroundings are set to periodic conditions to simulate the anti-reflection effect of large-area

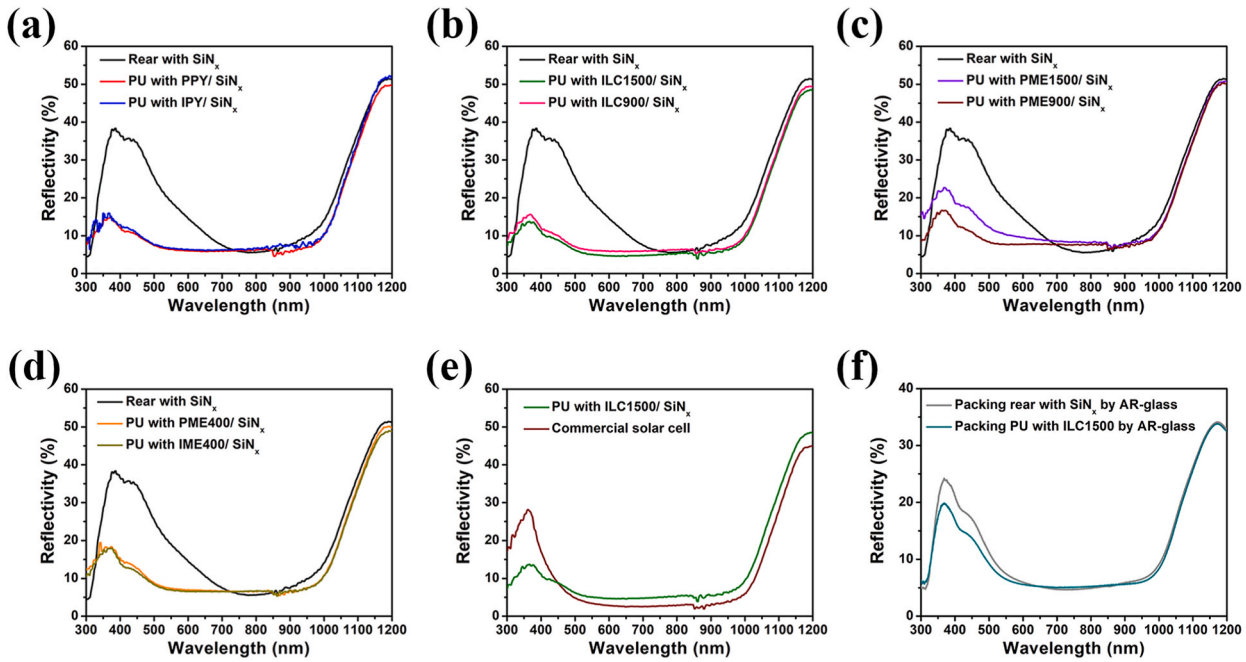

Fig. 4. Comparison of reflectance spectrum between PU with different morphologies and blank groups. (a) shows the PU with PPY and IPY, (b) shows the ILC1500 and ILC900, (c) shows the PME1500 and PME900, (d) shows the PME400 and IME400, (e) shows the comparison between ILC1500 and commercial solar cells, and (f) shows the comparison between packing the ILC1500 and blank group by AR-glass.

Table 3
Comparison of different anti-reflection structures.

AR Coating Material	ARC Structure	Fabrication Technology	Reflectance (%)	Wavelength Range (nm)	Reference
Polyurethane	Inverted lace cones	Soft imprint lithography	~8.71	300–1200	This work
ZnO	Nanorod array	Chemical bath deposition	15.9	300–1200	[41]
TiO_2	Thin film	Atmospheric pressure chemical vapor deposition	8.61	300–1150	[42]
Epoxy resin	Biomimetic diodon-skin nanothorn (DSNT) epoxy resin ARC	Soft imprint lithography	~15.8	300–1100	[43]
PDMS	Tappered nanoholes (NHs)	Soft lithography	~7.1	350–800	[44]
Polystyrene	Pyramid-arrayed PS film	Microinjection Compression molding	~5	400–900	[45]

inverted lace cones. As shown in Fig. 5(b), according to the SEM images, the maximum opening of ILC1500 is 1.8 μm, the depth is 1 μm and the average lace quantity is 10. The maximum opening of ILC900 is 1.3 μm, the depth is 650 nm and the average lace quantity is 6. The grid is divided as shown in Fig. 5(c), with the maximum grid not exceeding 1/6 of the minimum wavelength of 300 nm.

After global calculation, the global reflection spectrum for ILC1500 and ILC900 are shown in Fig. 5(d). The wide-band anti-reflection effect in the visible and part of the near-infrared spectrum can be found clearly. The anti-reflection effect of ILC1500 is better than that of ILC900, which is consistent with experimental results. When the wavelength of the incident into the ILC1500 is 400 nm, 500 nm, 550 nm, 650 nm, and 750 nm respectively, the electrical modulus intensity distributions in the XZ section are shown in Fig. 5 (e). Since ILC1500 is symmetrical about X-axis and Y-axis, the electrical modulus intensity distribution of the XZ section can represent the overall electrical modulus intensity distribution. When the incident wavelength is 400 nm, the light trapping effect of ILC1500 is poor, and the electrical modulus intensity is largely uniform throughout the anti-reflection structure region. However, as the wavelength increases, the ILC1500 structure exhibits a wide-band light trapping effect. When the incident wavelength is 500 nm, 550 nm, 650 nm, and 750 nm, respectively, the electrical modulus intensity of the incident electromagnetic waves is significantly stronger in the inverted lace cone region than in the other area, indicating that the light trapping effect of the incident electromagnetic waves are produced by the inverted lace cone light trapping structure. The dual role of SiN_x anti-reflection film and light trapping structure leads to a wide band of 500–1000 nm of low reflectivity, plane SiN_x itself the anti-reflection effect in the wavelength of 500–750 nm gradually enhanced, resulting in the response to the anti-reflection effect produced by the PU anti-reflection structure is diminished and the electric field strength of the structural area of the PU is also correspondingly become smaller. The results show that the anti-reflection effect of different texture structures can be evaluated using COMSOL multiphysics field finite element simulation, which is

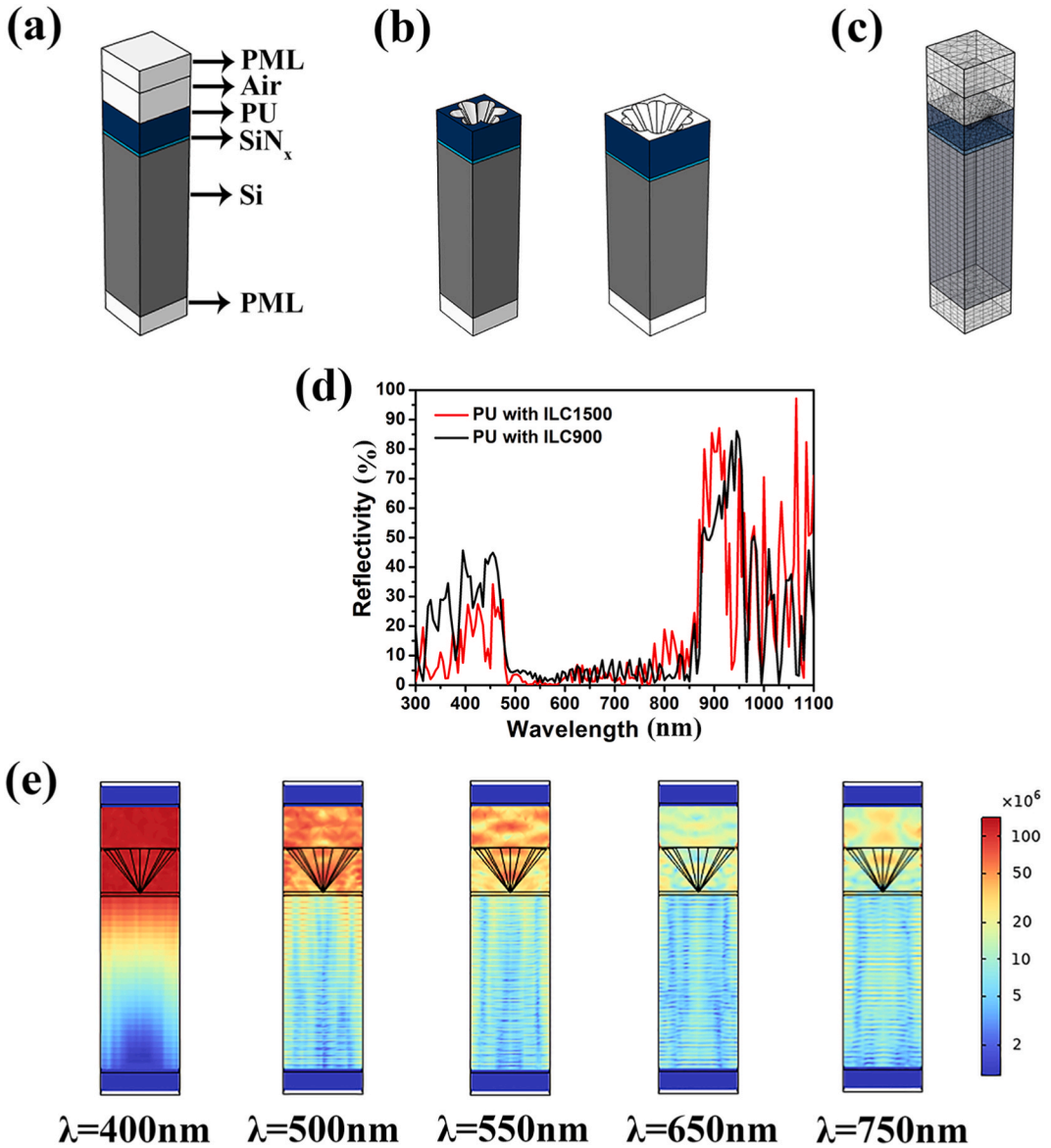

Fig. 5. (a), (b), and (c) show COMSOL optical simulation schematic diagrams, (d) shows the global reflectance calculation results of ILC1500 and ILC900, and (e) shows the intensity distribution of electrical modulus at different wavelengths of ILC1500.

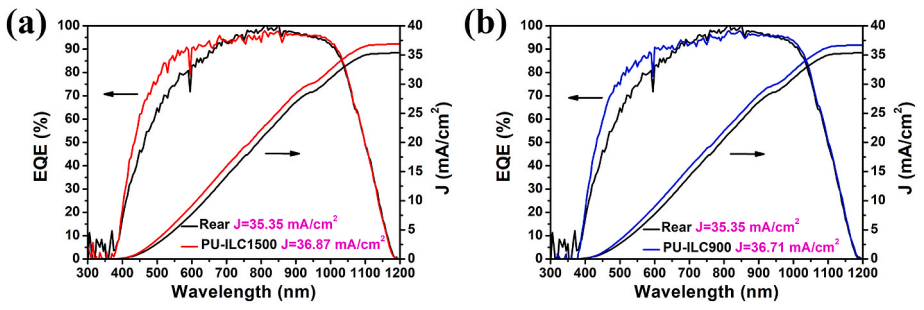

Fig. 6. (a) and (b) show the comparison of EQE and integrated current between the original sample and the samples with the ILC1500 and ILC900, respectively.

beneficial to guide the design of different texture structures.

To evaluate the impact of the prepared textures on the electrical performance of the solar cells. The external quantum efficiency of the blank back surface sample and two different texture samples in the range of 300–1200 nm are tested and their integral currents are calculated, as shown in Fig. 6. The main EQE gain range is consistent with the reflection spectrum. Compared to the original rear solar cells, the integrated current density of ILC1500 increased by 1.52 mA/cm^2(4.30%), and that of ILC900 increased by 1.36 mA/cm^2(3.85%). The gain of ILC1500 is better than that of ILC900, which is consistent with the reflection spectrum and COMSOL simulation results. When the front of the solar cell is a flat SiN_x layer, the preparation of a PU textured structure on it is also expected to yield a superior anti-reflection effect and produce an integrated current gain.

Using a large silicon wafer template, a PU layer with a random positive pyramid morphology on the backside of a 165 × 165 cm PERC bi-facial solar cell is successfully fabricated. This demonstrates the potential for industrial production of the nanoimprint method proposed in this article. As the soft nanoimprint technology iterates and scales up, its production costs will drop rapidly.

4. Conclusion

In order to overcome the disadvantages of the acid-alkali textured method of crystalline silicon solar cells, the high refractive index PU is prepared into different light trapping structures on the surface of the SiN_x layer by using soft nanoimprint lithography. Among them, the inverted lace cones produced by transferring the A1500 template resulted in a weighted average reflectance of 8.71% at 300–1200 nm bands on the back surface of the PERC bi-facial solar cells. Meanwhile, its integrated current density is increased by 4.05%. COMSOL optical simulation also demonstrates the feasibility of this method. The notable advantages of this method include its ability to transform various complex morphologies, low surface recombination on the surface of silicon wafers, no interference with the electrical performance of the solar cells, and fast, convenient, and pollution-free preparation. It is suitable for all types of novel structural crystalline silicon solar cells and thin film solar cells, which have great potential for development.

Author contribution statement

Shengxuan Wang: Conceived and designed the experiments; Performed the experiments; Analyzed and interpreted the data; Wrote the paper.

Hao Cui: Conceived and designed the experiments.

Sijia Jin: Performed the experiments.

Xiaodong Pi: Haiyan He: Chunhui Shou: Deren Yang: Contributed reagents, materials, analysis tools or data.

Lei Wang: Analyzed and interpreted the data; Contributed reagents, materials, analysis tools or data; Wrote the paper.

Data availability statement

Data will be made available on request.

Declaration of competing interest

The authors declare that they have no known competing financial interests or personal relationships that could have appeared to influence the work reported in this paper.

Acknowledgment

This work was supported by the National Key RD Program of China (No. 2020YFB1506502, 2018YFB1500300), Open Project of Key Laboratory of Solar Energy Utilization & Energy Saving Technology of Zhejiang Province (No. ZJS-OP-2020-01), National Science Foundation of China (No. 61721005), and Key Project of Zhejiang Province (No. 2021C01170).

References

[1] A. Allouhi, S. Rehman, M.S. Buker, Z. Said, Up-to-date literature review on Solar PV systems: technology progress, market status and R&D, J. Clean. Prod. 362 (2022), https://doi.org/10.1016/j.jclepro.2022.132339.

[2] Taesoo D. Leea, Abasifreke U. Ebong, A review of thin film solar cell technologies and challenges, Renew. Sustain. Energy Rev. 70 (2017) 1286–1297, https://doi.org/10.1016/j.rser.2016.12.028.

[3] N. Shanmugam, R. Pugazhendhi, R. Madurai Elavarasan, P. Kasiviswanathan, N. Das, Anti-Reflective coating materials: a holistic review from PV perspective, Energies 13 (2020), https://doi.org/10.3390/en13102631.

[4] Q.S. Chen, Y.P. Liu, W. Chen, Y. Zhao, J.T. Wu, Y. Wang, X.L. Du, Different silicon crystal face index of inverted pyramid structure, Acta Phys. Sin. 67 (2018), https://doi.org/10.7498/aps.67.20181275.

[5] B. Meinel, T. Langner, P. Preis, T. Sieber, E. Wefringhaus, J. Acker, A two-step acidic texturization procedure for the manufacture of low-reflective multi-crystalline silicon solar wafer, Sol. Energy 193 (2019) 395–402, https://doi.org/10.1016/j.solener.2019.09.051.

[6] J. Oh, H.C. Yuan, H.M. Branz, An 18.2%-efficient black-silicon solar cell achieved through control of carrier recombination in nanostructures, Nat. Nanotechnol. 7 (2012) 743–748, https://doi.org/10.1038/nnano.2012.166.

[7] Hirotoshi Torii, Hiura Mitsuru, Yukio Takabayashi, Kimura Atsushi, Yoshio Suzaki, Ito Toshiki, Yamamoto Kiyohito, Byung Jin Choi, Estrada Teresa, Nanoimprint lithography: today and tomorrow, Proc. SPIE 12054 (2022). https://doi:10.1117/12.2615740.

[8] M.M. Tavakoli, A. Simchi, R. Tavakoli, Z. Fan, Organic halides and nanocone plastic structures enhance the energy conversion efficiency and self-cleaning ability of colloidal quantum dot photovoltaic devices, J. Phys. Chem. C 121 (2017) 9757–9765, https://doi.org/10.1021/acs.jpcc.7b02394.

[9] K.H. Tsui, Q. Lin, H. Chou, Q. Zhang, H. Fu, P. Qi, Z. Fan, Low-cost, flexible, and self-cleaning 3D nanocone anti-reflection films for high-efficiency photovoltaics, Adv Mater 26 (2014) 2805–2811, https://doi.org/10.1002/adma.201304938.

[10] J.H. Lim, J.W. Leem, J.S. Yu, Solar power generation enhancement of dye-sensitized solar cells using hydrophobic and antireflective polymers with nanoholes, RSC Adv. 5 (2015) 61284–61289, https://doi.org/10.1039/c5ra10269c.

[11] Y. Lin, Z. Xu, D. Yu, L. Lu, M. Yin, M.M. Tavakoli, X. Chen, Y. Hao, Z. Fan, Y. Cui, D. Li, Dual-layer nanostructured flexible thin-film amorphous silicon solar cells with enhanced light harvesting and photoelectric conversion efficiency, ACS Appl. Mater. Interfaces 8 (2016) 10929–10936, https://doi.org/10.1021/acsami.6b02194.

[12] Y.J. Peng, H.X. Huang, H. Xie, Rapid fabrication of antireflective pyramid structure on polystyrene film used as protective layer of solar cell, Sol. Energy Mater. Sol. Cells 171 (2017) 98–105, https://doi.org/10.1016/j.solmat.2017.06.013.

[13] Y. Xia, Z. Zhang, M. Gao, Y. Zheng, L. Chen, Y. Si, S. Mei, Enhancement in photoelectric performance of dye-sensitized solar cells with inverted pyramid structures based on nanoimprint lithography, AIP Adv. 11 (2021), https://doi.org/10.1063/5.0054147.

[14] G. Li, H. Li, J.Y. Ho, M. Wong, H.S. Kwok, Nanopyramid structure for ultrathin c-Si tandem solar cells, Nano Lett. 14 (2014) 2563–2568, https://doi.org/10.1021/nl500366c.

[15] A. Jacobo-Martín, J.J. Hernández, E. Solano, M.A. Monclús, J. Carlos Martínez, D.F. Fernandes, P. Pedraz, J.M. Molina-Aldareguia, T. Kubart, I. Rodríguez, Resilient moth-eye nanoimprinted antireflective and self-cleaning TiO_2 sputter-coated PMMA films, Appl. Surf. Sci. 585 (2022), https://doi.org/10.1016/j.apsusc.2022.152653.

[16] S. Jang, S.M. Kang, M. Choi, Multifunctional moth-eye TiO_2/PDMS pads with high transmittance and UV filtering, ACS Appl. Mater. Interfaces 9 (2017) 44038–44044, https://doi.org/10.1021/acsami.7b15502.

[17] S.Y. Heo, J.K. Koh, G. Kang, S.H. Ahn, W.S. Chi, K. Kim, J.H. Kim, Bifunctional moth-eye nanopatterned dye-sensitized solar cells: light-harvesting and self-cleaning effects, Adv. Energy Mater. 4 (2014), https://doi.org/10.1002/aenm.201300632.

[18] C. Fang, Z. Yang, J. Zhang, Y. Zhuang, S. Liu, X. He, Y. Zhang, Biomimetic diodon-skin nanothorn polymer antireflection film for solar cell applications, Sol. Energy Mater. Sol. Cells 206 (2020), https://doi.org/10.1016/j.solmat.2019.110305.

[19] Y. Wan, K.R. McIntosh, A.F. Thomson, Characterisation and optimisation of PECVD SiNx as an antireflection coating and passivation layer for silicon solar cells, AIP Adv. 3 (2013), https://doi.org/10.1063/1.4795108.

[20] K. Isakov, C. Kauppinen, S. Franssila, H. Lipsanen, Superhydrophobic antireflection coating on glass using grass-like alumina and fluoropolymer, ACS Appl. Mater. Interfaces 12 (2020) 49957–49962, https://doi.org/10.1021/acsami.0c12465.

[21] M. Wang, H. He, C. Shou, H. Cui, D. Yang, L. Wang, Anti-reflection effect of large-area ZnO nano-needle array on multi-crystalline silicon solar cells, Mater. Sci. Semicond. Process. 138 (2022), https://doi.org/10.1016/j.mssp.2021.106299.

[22] S. Tomaru, Y. Murakoshi, M. Michiguchi, H. Kohno, K. Yamauchi, H. Kosimizu, A. Yamauchi, J. Nakamura, Practical high refractive index resin useable for near IR and visible wavelengths, in: Conference on Organic Photonic Materials and Devices XXI, CA, San Francisco, 2019, https://doi.org/10.1117/12.2512019.

[23] B. Cai, T. Kaino, O. Sugihara, Sulfonyl-containing polymer and its alumina nanocomposite with high Abbe number and high refractive index, Opt. Mater. Express 5 (2015) 1210–1216, https://doi.org/10.1364/ome.5.001210.

[24] K. Mazumder, H. Komber, E. Bittrich, K. Uhlig, B. Voit, S. Banerjee, Sulfur-rich polyimides containing bis(3-(trifluoromethyl)phenyl)thiophene for high-refractive-index applications, Macromolecules 55 (2022) 9766–9779, https://doi.org/10.1021/acs.macromol.2c01384.

[25] H. Kim, B.C. Ku, M. Goh, H. Yeo, H.C. Ko, N.H. You, Synthesis and characterization of phosphorus- and sulfur-containing aromatic polyimides for high refractive index, Polymer 136 (2018) 143–148, https://doi.org/10.1016/j.polymer.2017.12.052.

[26] Xu Zhang, Aili Yang, Zhiguo Jiang, Jun Zhang, Ming Yao, Synthesis of isothiocyanate and mercaptan and research progress on sulfur-containing polyurethane resin in the field of optical len, N. Chem. Mater. 49 (2021) 265–268.

[27] Z. Xu, H. Huangfu, X. Li, H. Qiao, W. Guo, J. Guo, H. Wang, Role of nanocone and nanohemisphere arrays in improving light trapping of thin film solar cells, Opt Commun. 377 (2016) 104–109, https://doi.org/10.1016/j.optcom.2016.05.050.

[28] Z. Xu, H. Qiao, H. Huangfu, X. Li, J. Guo, H. Wang, Optical absorption of several nanostructures arrays for silicon solar cells, Opt Commun. 356 (2015) 526–529, https://doi.org/10.1016/j.optcom.2015.08.069.

[29] K. Kluczyk, C. David, J. Jacak, W. Jacak, On modeling of plasmon-induced enhancement of the efficiency of solar cells modified by metallic nano-particles, Nanomaterials 9 (2018), https://doi.org/10.3390/nano9010003.

[30] C. Wang, S. Zhao, F. Bian, D. Du, C. Wang, Z. Xu, Absorption enhancement of ultrathin crystalline silicon solar cells with frequency upconversion nanosphere arrays, Commun. Theor. Phys. 72 (2020), https://doi.org/10.1088/1572-9494/ab5451.

[31] Sijia Guo, Caixing Hu, Haifeng Zhang, Unidirectional ultrabroadband and wide-angle absorption in graphene-embedded photonic crystals with the cascading structure comprising the Octonacci sequence, J. Opt. Soc. Am. B 37 (2020) 2678–2687, https://doi.org/10.1364/JOSAB.399048.

[32] Qu Jia, Hao Pan, Yuanzhe Sun, Haifeng Zhang, Multitasking device regulated by the gravity field: broadband anapole-excited absorber and linear polarization converter, Ann. Phys. 534 (2022), 2200175, https://doi.org/10.1002/andp.202200175.

[33] Zihan Guo, Chengjing Gao, Haifeng Zhang, Direction-dependent janus metasurface supported by waveguide structure with spoof surface plasmon polariton modes, Adv. Mater. Technol. 8 (2023), 2200435, https://doi.org/10.1002/admt.202200435.

[34] T. Sugiura, S. Matsumoto, N. Nakano, Bifacial PERC solar cell designs: bulk and rear properties and illumination condition, IEEE J. Photovoltaics 10 (2020) 1538–1544, https://doi.org/10.1109/jphotov.2020.3013987.

[35] COMSOL Multiphysics® V. 6.0. cn.comsol.Com. COMSOL AB, Stockholm, Sweden.

[36] Guiming Zhang, Study on TTT-η Diagram and Curing Molding of High-Refractive Polyurethane Optical Resin, Donghua University, 2021.

[37] IEC, Photovoltaic Devices—Part 3. Measurement Principles for Terrestrial Photovoltaic (PV) Solar Devices with Reference Spectral Irradiance Data, International Electrotechnical Commission, 2008.

[38] Fan Shen, The Compound of High Refractive Index Optical Resin—Characterization, Synthesis and Properties, Wuhan Polytechnic University, 2016.

[39] Y. Wu, J. Li, Z.Q. Zhang, C.T. Chan, Effective medium theory for magnetodielectric composites: beyond the long-wavelength limit, Phys. Rev. B 74 (2006), 085111, https://doi.org/10.1103/PhysRevB.74.085111.

[40] Laura Stevens, Höhn Oliver, Mario Hanser, Nico Tucher, Claas Müller, Stefan Glunz, Benedikt Bläsi, Impact of the refractive index on coupling structures for silicon solar cells, J. Photon. Energy 11 (2021), https://doi.org/10.1117/1.JPE.11.027001.

[41] Yazhou Qu, Xuan Huang, Yanqiu Li, Guanhua Lin, Bin Guo, Dengyuan Song, Qijin Cheng, Chemical bath deposition produced ZnO nanorod arrays as an antireflective layer in the polycrystalline Si solar cells, J. Alloys Compd. 698 (2017) 719–724, https://doi.org/10.1016/j.jallcom.2016.12.265.

[42] D. Hocine, M.S. Belkaid, M. Pasquinelli, L. Escoubas, J.J. Simon, G.A. Rivière, A. Moussi, Improved efficiency of multicrystalline silicon solar cells by TiO_2 antireflection coatings derived by APCVD process, Mater. Sci. Semicond. Process. 16 (2013) 113–117, https://doi.org/10.1016/j.mssp.2012.06.004.

[43] Chaolong Fang, Zhitong Yang, Jian Zhang, Youyi Zhuang, Siyuan Liu, Xin He, Yaoju Zhang, Biomimetic diodon-skin nanothorn polymer antireflection film for solar cell applications, Sol. Energy Mater. Sol. Cells (2019), https://doi.org/10.1016/j.solmat.2019.110305.

[44] Joo Ho Lim, Jung Woo Leem, Jae Su Yu, Solar power generation enhancement of dyesensitized solar cells using hydrophobic and antireflective polymers with nanoholes, RSC Adv. 5 (2015) 61284–61289, https://doi.org/10.1039/c5ra10269c.

[45] Yujiang Peng, Hanxiong Huang, Heng Xie, Rapid fabrication of antireflective pyramid structure on polystyrene film used as protective layer of solar cell, Sol. Energy Mater. Sol. Cells 171 (2017) 98–106, https://doi.org/10.1016/j.solmat.2017.06.013.